Research Square

Preprints are preliminary reports that have not undergone peer review.
They should not be considered conclusive, used to inform clinical practice,
or referenced by the media as validated information.

Active Flow Control over a NACA 4412 Airfoil Using Optimized DBD Plasma Actuators: An ANFIS-Assisted CFD Optimization Framework

Morteza Bayati

m.bayati.aut@gmail.com

Urmia University of Technology

Article

Keywords: Plasma Actuator, ANFIS, Active Flow Control, Aerodynamic Performance

Posted Date: November 20th, 2026

DOI: https://doi.org/10.21203/rs.3.rs-11504842/v1

License: This work is licensed under a Creative Commons Attribution 4.0 International License.
Read Full License

Additional Declarations: No competing interests reported.

Active Flow Control over a NACA 4412 Airfoil Using Optimized DBD Plasma Actuators: An ANFIS-Assisted CFD Optimization Framework

Morteza Bayati
Faculty of Mechanical Engineering, Department of Aerospace Engineering, Urmia University of Technology, Urmia, Iran.
Corresponding author: Morteza Bayati
Email: m.bayati.aut@gmail.com

Abstract
This study introduces a hybrid optimization framework for active flow control over airfoils by integrating Computational Fluid Dynamics (CFD) with an Adaptive Neuro-Fuzzy Inference System (ANFIS). The goal is to enhance airfoil performance using Dielectric Barrier Discharge Plasma Actuators (DBD-PAs). A NACA 4412 airfoil at a Reynolds number of 6.86×10^5 served as the benchmark. An ANFIS surrogate was trained on CFD simulations and then employed as the objective function within an optimization framework to identify optimal actuator strength and placement beyond the simulated design space. The objective function is to simultaneously increase lift, reduce drag, and make the pitching moment coefficient more positive. The optimization identified a configuration with the actuator placed at 30% chord. At the stall condition, this optimal configuration produced a 26.5% increase in lift, a 27.6% decrease in drag, and a more positive pitching moment coefficient at post-stall angles. Notably, strategically placed actuators near the leading edge demonstrated significant efficacy in suppressing the low-pressure vortex on the suction side, leading to a substantial reduction in drag at high angles of attack. Conversely, actuators placed near the trailing edge exhibited a counterproductive effect, whereas at low angles of attack rearward actuation remained beneficial for aerodynamics enhancement.

Keywords: Plasma Actuator, ANFIS, Active Flow Control, Aerodynamic Performance

1. Introduction

Flow-control methods have gained considerable attention across various scientific fields because of their capability to enhance performance and manage airflow in aerodynamic systems. These methods are generally characterized as either passive or active. In passive methods, flow control is accomplished through physical modifications to the body without using external energy, while in active methods, external energy is used without altering the structure. Furthermore, hybrid methods that simultaneously employ both active and passive approaches are also used [1]. Among passive methods, vortex generators can be mentioned, while among active methods, plasma actuators, suction and blowing, and the Coanda effect can be cited [2]. The active flow-control methods provide an effective means of modifying an object's aerodynamic behavior without relying on mechanical moving components. These devices generate localized flow disturbances that interact with the surrounding airflow, enabling precise control of flow separation, boundary-layer behavior, and aerodynamic forces on aircraft wings, wind-turbine blades, and similar surfaces [3]. The principal objective of flow control is to mitigate or delay boundary layer separation. By reducing the extent of the separated flow region, these techniques promote pressure recovery over the aerodynamic surface, ultimately enhancing lift production and delaying the onset of stall. Among active flow control methods, plasma actuators are distinguished by their fast response time, no need for surface modifications, and the absence of moving mechanical parts,

which has led to their application in optimizing industries, including suppressing massive flow separation over wind turbine blades to reduce the transient aerodynamic loads acting on the turbine blades [4], reducing airfoil noise [5] and controlling the flow over a hypersonic airfoil [6]. The physical phenomenon resulting from DBD is the generation of a body force, which appears as a source term in the governing equations due to momentum injection. This enables control of the flow to prevent or reduce surface separation [7]. DBD plasma actuators consist of two electrodes, one exposed to air and the other enclosed by a dielectric material. Figure 1 schematically shows a typical DBD-PA. The electrodes, when driven by a sufficiently high amplitude voltage, cause ionization of the air above the encapsulated electrode. The ionized air particles, accelerated by the electric field, apply a body force to the neutral air near the actuator, which ultimately leads to the generation of an induced flow [8]. Experimental studies have established two primary operational modalities for DBD plasma actuators: steady and unsteady (or pulsed) actuation. Under steady operation, the actuator produces a continuous wall jet through electrohydrodynamic body forces. This steady momentum injection thickens the momentum boundary layer directly augmenting the velocity of particles in the near wall region. This added energy enhances their streamwise momentum, allowing them to penetrate further into regions of adverse pressure gradient and effectively suppress separation inception. It has also been shown that using multiple steady actuators in series can improve the induced flow of plasma actuators [9]. In contrast, unsteady actuation operates on a fundamentally different principle: the periodic excitation of the flow field. This excitation generates coherent vortex structures that enhance momentum transport into the separated shear layer. The effectiveness of this control strategy depends strongly on the actuation frequency, which must be tuned to a characteristic flow timescale to achieve optimal separation control via a resonance mechanism. Because separated flows are inherently chaotic, plasma actuators should be placed outside the separation region; ideally, they are located near the separation point (either upstream or downstream) to provide more effective separation control [10]. Active flow control faces several challenges: selecting optimal electrode geometry, dielectric properties, actuation frequency and amplitude, and mounting location. Additionally, numerical errors, modeling uncertainties, and issues introduced by optimization algorithms complicate reliable design and performance prediction [11]. Much research has been conducted on plasma actuators to increase their performance, adaptability, and more accurate physical simulation for aerodynamic actuation [12], using horseshoe and serpentine plasma actuators [13], examination of linear and nonlinear effects of voltage and frequency variation [14], and strategies for selecting suitable plasma actuator placement [15], all aimed at improving aerodynamic performance. Jukes [16] reported a 300% increase in lift on a cylinder at 1.6 m/s and a 69% reduction in drag on a NACA0024 airfoil at 10 m/s. In their experimental work, the flow structure was studied using time-resolved particle image velocimetry and flow visualization, and the lift and drag forces were measured with a two-component force balance. Based on their experimental results, they concluded that the effect of the plasma actuator causes a breakdown of the shear layer, which leads to flow reattachment. Subsequently, secondary vortices are released into the near wake, and the strength of these secondary vortices depends on the orientation angle of the plasma actuator. Zhang [17] improved lift by 98.8% on an SC(2)-0714 airfoil at freestream velocities of 15 to 60 m/s. Daud [18] reported a 25% lift increase on a NACA0015 airfoil at 10 m/s, and Mahdavi [19] reported a 13% lift increase on an airfoil at 3.9 m/s. Tang [20] observed a 270% lift increase on a cylinder at low Reynolds numbers. Chen [21], Taleghani [22], and Yarusevych [23] worked, respectively, on a D-shaped body, the NLF0414 airfoil, and a separation bubble on the NACA0012 airfoil. Bei [24] found a 7% improvement in lift on the NLF0416 airfoil at Mach 0.1; Phan [25]

reported a 70% increase in lift on the NACA0012 airfoil at 6 m/s; and Abdelraouf [26] achieved a 6.1% improvement in lift on a flat plate and the NACA0012 airfoil at Mach 0.3. In the work of Huang [27] and Kayvanpour [28], the effect of plasma actuators on the flow over a two-dimensional, incompressible, and turbulent pitching airfoil was considered. Zavarian [29] found numerically that placing plasma actuators nearer the leading edge suppresses low-pressure vortex growth and lowers drag, highlighting the strong influence of leading-edge vortices on airfoil performance. Yu [30], using LES, showed that plasma–flow interaction produces eddies via vortex expansion, promoting large-scale vortices that drive early flow-control dynamics; they reported optimal control when actuation frequency is high and close to the natural frequency of the unforced separated shear layer.

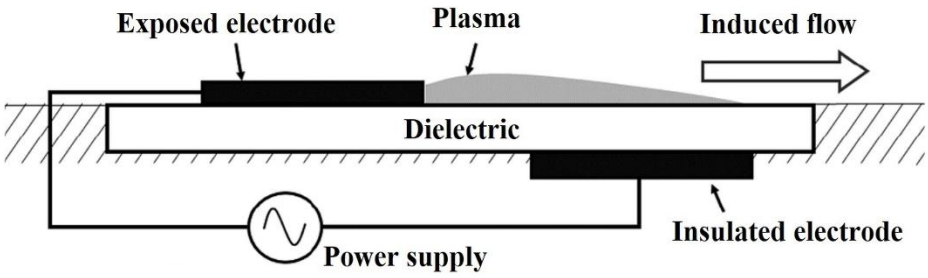

Fig. 1 Schematic of a DBD plasma actuator

Numerical and experimental studies indicate that plasma-actuator performance is highly sensitive to many factors, including installation location, actuator count, jet orientation, voltage amplitude, frequency, and electrode geometry. Despite extensive parametric investigations, a general predictive framework applicable across varied flow conditions and scales remains lacking. The optimum actuator location changes with flow regime, but a predictive framework for identifying this transition has not been established. This gap motivates the development of data-driven surrogate models that can efficiently explore high-dimensional design spaces. Among various machine learning approaches, ANFIS offers distinct advantages: (1) interpretability through fuzzy rules, (2) robustness to incomplete datasets, and (3) ability to capture strongly nonlinear input-output relationships. These features make ANFIS particularly suitable for aerodynamic optimization, where lift, drag, and pitching moment depend nonlinearly on flow conditions and actuator parameters.

This study introduces a CFD–ANFIS optimization framework for active flow control on a NACA 4412 airfoil using DBD plasma actuators. Unlike prior studies that rely on exhaustive parametric sweeps or use metamodels merely for interpolation, the proposed approach employs the ANFIS surrogate as the objective function within an optimization algorithm to locate optimal actuator configurations beyond the simulated design space. The ANFIS-predicted optimum is then verified by an additional CFD simulation. The key contributions of this work are: (1) development and systematic validation of an ANFIS surrogate model for DBD plasma-actuator flow control on a NACA 4412 airfoil; (2) demonstration that ANFIS-assisted optimization can identify effective actuator configurations with a computational cost substantially lower than an exhaustive parametric sweep; (3) identification of a critical chordwise placement limit of approximately 30% beyond which aerodynamic performance degrades sharply in both pre- and post-stall regimes; and (4) clear distinction between the lift-enhancement mechanisms associated with leading-edge versus trailing-edge actuation.

The remainder of this paper is organized as follows. The governing equations and numerical solution method are first presented and validated against experimental results. Next, the plasma-actuator modeling approach is described and compared with experimental data. Subsequently, the neural network methodology and its validation are discussed. Finally, optimal actuator deployment scenarios for maximizing aerodynamic performance are analyzed.

2. Numerical method

2.1. Governing equations

In this study, the two dimensional, incompressible, and unsteady Reynolds averaged Navier Stokes (URANS) equations were used according to equations 1 and 2.

$$\frac{\partial u_i}{\partial x_i} = 0 \tag{1}$$

$$\frac{\partial u_i}{\partial t} + u_j \frac{\partial u_i}{\partial x_j} = -\frac{1}{\rho}\frac{\partial}{\partial x_i} + \frac{\partial}{\partial x_j}\left[\nu\left(\frac{\partial u_i}{\partial x_j} + \frac{\partial u_j}{\partial x_i}\right) - \left(\overline{\acute{u}_i \acute{u}_j}\right)\right] + \frac{F_i}{\rho} \tag{2}$$

In these equations x_i (i=1,2,3) represent the space cartesian coordinates, u represents the components of time averaged flow velocity and ú represents the components of fluctuating flow velocity. ν, p, and ρ represent the kinematic viscosity, time averaged pressure and density, respectively, and F is the body force.

A C-shaped structured grids with 273460 cells is employed to discretize the two-dimensional computational domain for higher accuracy. The overall grid plot and grid division close to the airfoil are displayed in Figure 2. When chord length (c) of airfoil is equal to 1 m, Reynolds number (Re) is 6.86×10^5 for U_∞=10 m/s. Finally, to guarantee y+ < 1, the first layer has a mesh height of 1.1×10^{-4} m. The calculation domain size is set as 40 times the chord length in the longitudinal direction and 20 times in the transverse direction. An incompressible unsteady 2D finite volume CFD solver is employed for URANS. The simulation was conducted using a pressure-based solver with the Semi Implicit Method for Pressure Linked Equations (SIMPLE) algorithm. The Transition SST model, based on the work of Dong [31], was selected as the turbulence model for modeling the transition Shear Stress terms. The transition SST model is based on SST k−ω transport equations coupled with two additional transport equations: one for intermittency γ and the other for the transition Reynolds number $Re_{\theta t}$ according to equations 3 and 4. The pressure, momentum, and turbulence transport equations are discretized using second-order spatial schemes.

$$\frac{\partial(\gamma u_j)}{\partial t} + \rho\frac{\partial(\gamma u_j)}{\partial x_j} = P\gamma_1 - E\gamma_1 + P\gamma_2 - E\gamma_2 + \frac{\partial}{\partial x_j}\left[\left(\mu + \frac{\mu_t}{\sigma_\gamma}\right)\frac{\partial \gamma}{\partial x_j}\right] \tag{3}$$

$$\frac{\partial(\tilde{R}e_{\theta t}u_j)}{\partial t} + \rho\frac{\partial(\tilde{R}e_{\theta t}u_j)}{\partial x_j} = P_{\theta t} + \frac{\partial}{\partial x_j}\left[\sigma_{\theta t}(\mu + \mu_t)\frac{\partial \tilde{R}e_{\theta t}}{\partial x_j}\right] \tag{4}$$

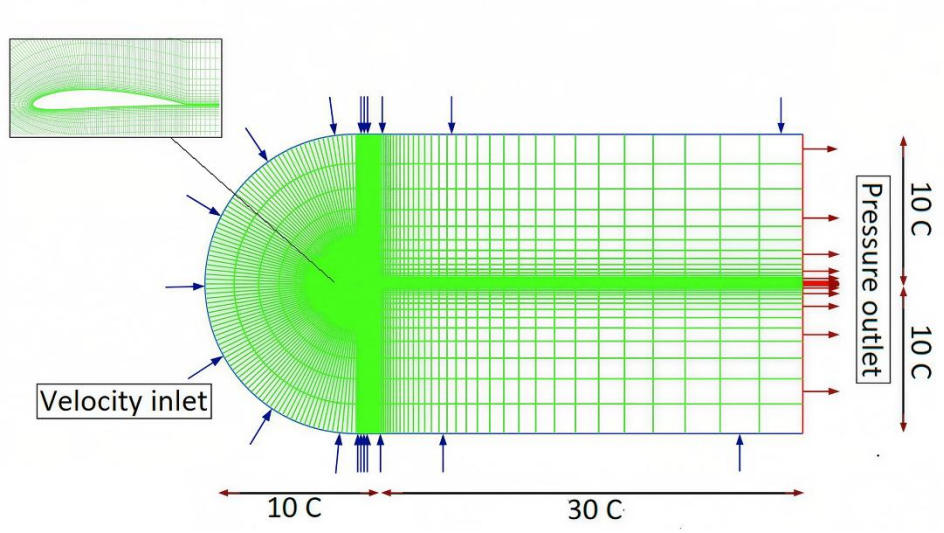

Fig. 2 grid plot around the computational domain

2.2. Grid independency study and time step sizing

The computational domain was discretized using a structured mesh, with refined prismatic layers implemented adjacent to the wall surfaces to accurately resolve boundary layer phenomena. A grid independence study was conducted using four mesh resolutions: 58,500, 78,150, 273,460, and 413,190 cells. Unsteady simulations were performed for each mesh until all residuals fell below 1×10^{-5}. Figure 3 compares the aerodynamic coefficients (Cl, Cd, Cm) across the four meshes. The difference between mesh #3 and #4 was less than 2%, while mesh #3 offered significantly lower computational cost. Therefore, mesh #3 (273,460 cells) was selected for all subsequent simulations.

A time step sensitivity analysis was also performed using three time steps: 0.0005, 0.001, and 0.002 s (Table 1). Reducing the time step from 0.001 to 0.0005 s changed the results by approximately 3%, while increasing it to 0.002 s changed the results by approximately 14%. Thus, a time step of 0.001 s was chosen, providing sufficient accuracy with reasonable computational cost.

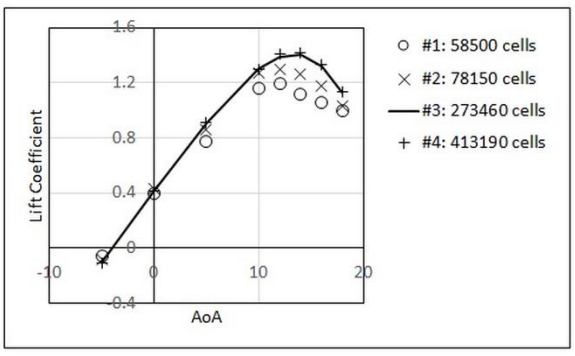

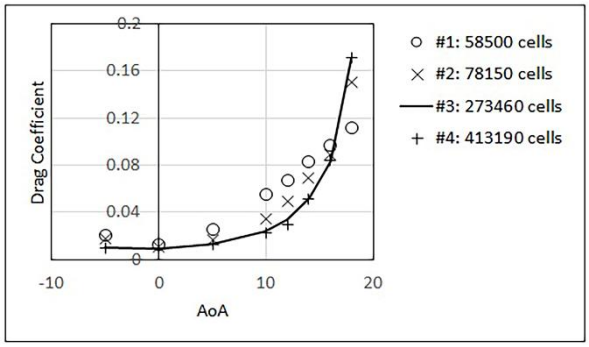

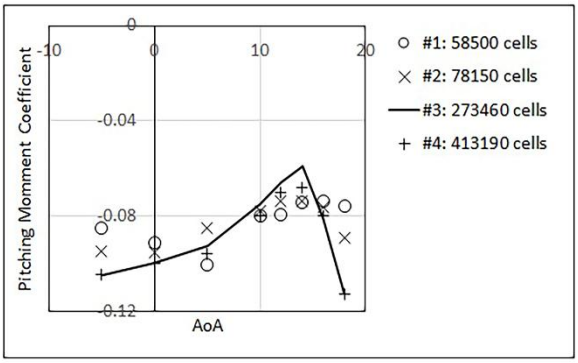

Fig. 3 Grid sensitivity analysis

Table 1 Sensitivity analyses of time step sizing

Time step	Cl	Cd	Cm
0.0005	1.401	0.054	-0.061
0.001	1.402	0.0522	-0.059
0.002	1.53	0.0599	-0.051

2.3. Validation of numerical solution method

To validate the numerical methodology employed in this study, the simulation results were compared against established experimental and numerical data. The experimental work of Storms and Jang [32] on the NACA 4412 airfoil was selected as the benchmark for this validation. A simulation was conducted for the clean airfoil configuration (without plasma actuation) using the Transition SST turbulence model to assess its capability to accurately capture the flow field characteristics. The close agreement between the present computational results and the reference data confirms the accuracy of the simulation approach and the suitability of the chosen turbulence model for this aerodynamic study.

Comparison plots of the lift coefficient versus angle of attack, and drag coefficient, and pitching moment coefficient versus Cl for the NACA 4412 airfoil without plasma actuation, together with experimental data [32] are presented at Figure 4. The numerical results exhibit close agreement with the experimental trends across all aerodynamic coefficients. A minor discrepancy of less than 6% is observed in the maximum lift coefficient (Cl max), which is attributable to the inherent challenges in modeling the unsteady, highly turbulent flow near stall conditions using URANS-based approaches. The agreement is notably strong at low angles of attack (AoA < 10°), while some deviations occur near and beyond stall, consistent with known limitations of turbulence models in predicting full separation dynamics.

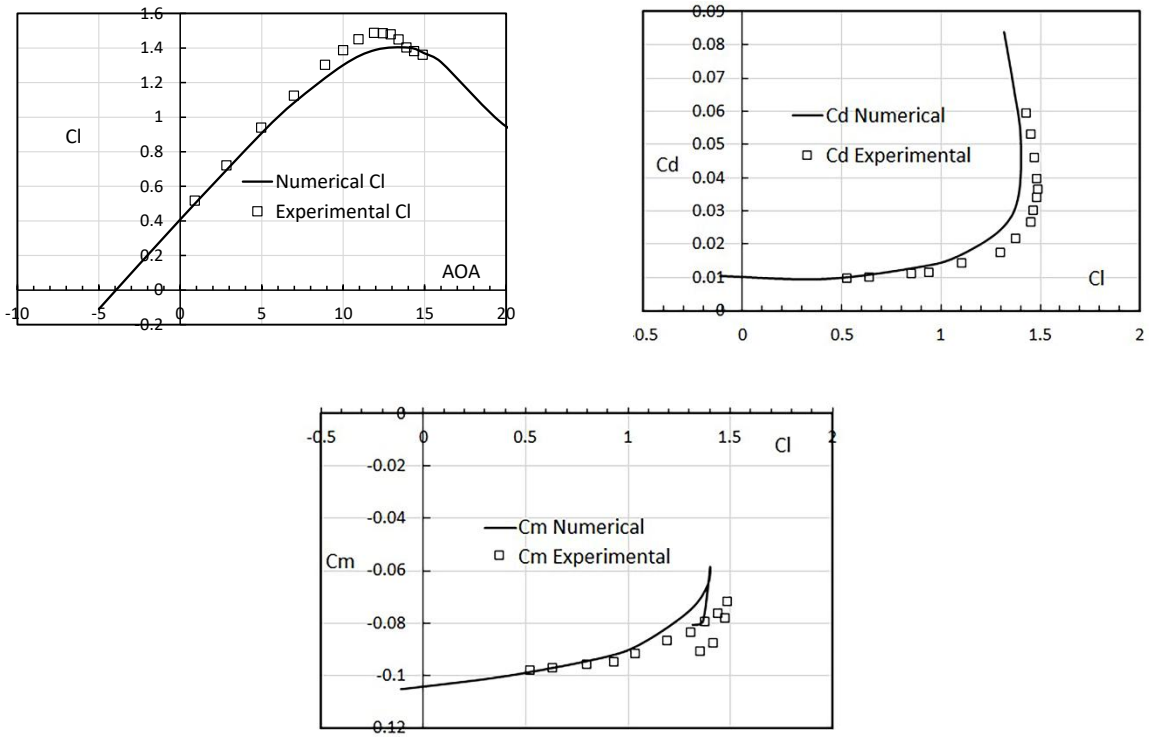

Fig. 4 Comparison of lift, drag, and pitching moment coefficients between present work and experimental data [32]

2.4. Plasma actuator

The influence of plasma actuators is modeled by incorporating a body force term into the governing flow equations. This force, denoted as F, is applied within a localized region corresponding to the actuator's position on the airfoil surface. When driven by a continuous or low-frequency alternating current signal, the actuator generates a relatively steady body force. These actuators enable precise airflow control with low energy consumption, enhancing flow stability by delaying boundary layer separation and attenuating turbulence. A significant advantage of this flow control technique is the achievement of improved aerodynamic performance without mechanical moving parts, thereby ensuring enhanced durability and reduced maintenance requirements. For the numerical implementation in this work, the body force model proposed by Shyy [33] is adopted. The body force in Equation (2) is calculated according to equations 5 to 10.

$$E = \left(|E| \frac{k_a}{\sqrt{k_a^2 + k_b^2}}, |E| \frac{k_b}{\sqrt{k_a^2 + k_b^2}}, 0 \right) \tag{5}$$

$$|E| = |E_0 - k_b x - k_a y| \tag{6}$$

$$F = \vartheta \rho_c e_c \Delta t E \tag{7}$$

$$E_0 = \frac{U_0}{d} \tag{8}$$

$$k_b = \frac{E_0 - E_b}{b} \tag{9}$$

$$k_a = \frac{E_0 - E_b}{a} \tag{10}$$

Where E is the electric field strength of plasma, E_0 is the maximum electric field strength, U_0 is the applied voltage, the constants of k_b and k_a are determined in such a way that the field strength is equal to the breakdown value at the plasma fluid boundary. e_c is the elementary charge, ϑ is the frequency of the applied voltage, and Δt is the discharge time. The values of the parameters in the equations 5 to 10 are taken from Jayaraman and Shyy [34]. E_b is the breakdown electric field strength of 30 kV/cm, a is the plasma height of 1.5 mm, b is the plasma width of 3 mm, and d is the distance between the two electrodes of 0.25 mm. The schematic of the plasma actuator is shown in Figure 5. The line A-B constitutes the plasma boundary using linear approximation. The electric field strength outside this line is not strong enough to ionize the air.
Since the required input is a body force in the Navier Stokes equations, it can be expressed by a relation. In this study, the body force per unit length varies with the applied voltage approximately according to equation 11 from reference [35]. In this relation U_0 is the input voltage in kV and F is the actuator force in mN/m.

$$F = 3.26U_0 - 17.32 \tag{11}$$

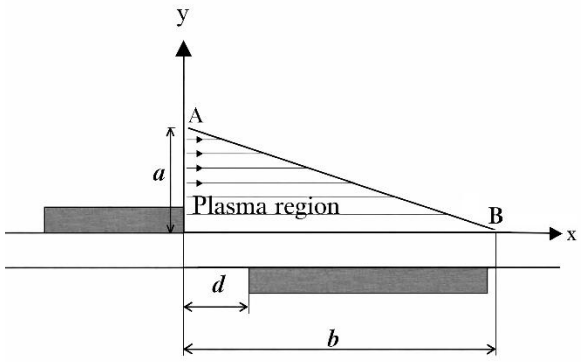

Fig. 5 The electric field strength and Plasma formation region

2.5. Validation of the Plasma Actuator Model

The plasma actuator model was validated against the experimental data of Roth [36] and the numerical results of Reference [33]. The validation study was conducted for a flat plate with a length of 20.5 mm in an airflow with a velocity of 5 m/s. The plasma actuator dimensions were specified as a length of 0.5 mm, with electrode heights of 0.1 mm (top) and 3 mm (bottom) on the dielectric surface, separated by a gap of 0.25 mm. The actuator was driven by an input voltage of 4 kV at a frequency of 3 kHz. Velocity profiles were compared at four streamwise measurement locations: ST-1 (8.25 mm upstream of the actuator), ST-2 (1 mm upstream), ST-3 (0.4 mm downstream), and ST-4 (3.8 mm downstream). As shown in Figure 6, the numerical results of the

present study show good agreement with the reference data, confirming the accuracy of the implemented plasma actuator model.

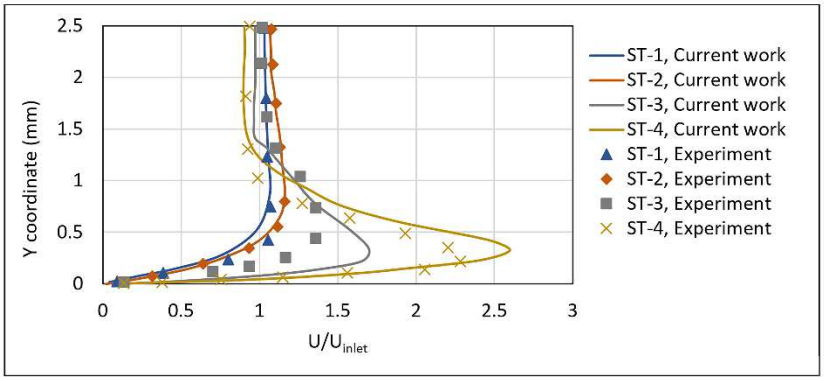

Fig. 6 Velocity profile in the presence of the DBD-PA on the flat plate from current work and experiment[33]

3. Adaptive Neuro-Fuzzy Inference System (ANFIS)

ANFIS is a hybrid intelligence technique that combines the interpretability of fuzzy logic with the learning capability of neural networks. Unlike purely statistical methods, ANFIS generates interpretable fuzzy rules that elucidate the influence of input parameters on outputs. It also demonstrates robust performance with incomplete datasets [37-40]. ANFIS combines fuzzy logic's transparent, rule-based handling of uncertainty with neural networks' adaptive learning, producing a hybrid model ideal for accurately capturing strongly nonlinear systems. This makes it especially suitable for aerospace problems, where lift, drag, and other performance metrics depend nonlinearly on flow conditions and geometry.

As shown in Figure 7, the ANFIS architecture comprises five layers: fuzzification, implication, normalization, defuzzification, and summation layer. The input signals are transferred to the first layer which is called the fuzzification layer. Different membership functions $(\mu_{Ai}(x), \mu_{Bi}(y), \dots)$ in this layer product membership grades from the input variables. The second layer is called the implication layer. Each fixed node in this layer states the rules and number of the Sugeno fuzzy inference system.

$$w_i = \mu_{Ai}(x).\mu_{Bi}(y) \quad i = 1, 2, \dots, n \tag{12}$$

The output of each node in this layer (w_i) is the product of the membership degrees from the previous layer. The third layer (normalization) computes the normalized ignition level for each rule ($\overline{w}_i$).

$$\overline{w}_i = w_i / \Sigma_1^n w_i \quad i = 1, 2, \dots, n \tag{13}$$

In the fourth layer referred to as the defuzzification layer, the normalized ignition level is multiplied by a specific function of inputs ($\overline{w}_i f_i$). Finally, there is a single node in the last layer (summation) which is indicated with $\sum$. The outputs of the nodes in the fourth layer are added together, and the final ANFIS output is calculated.

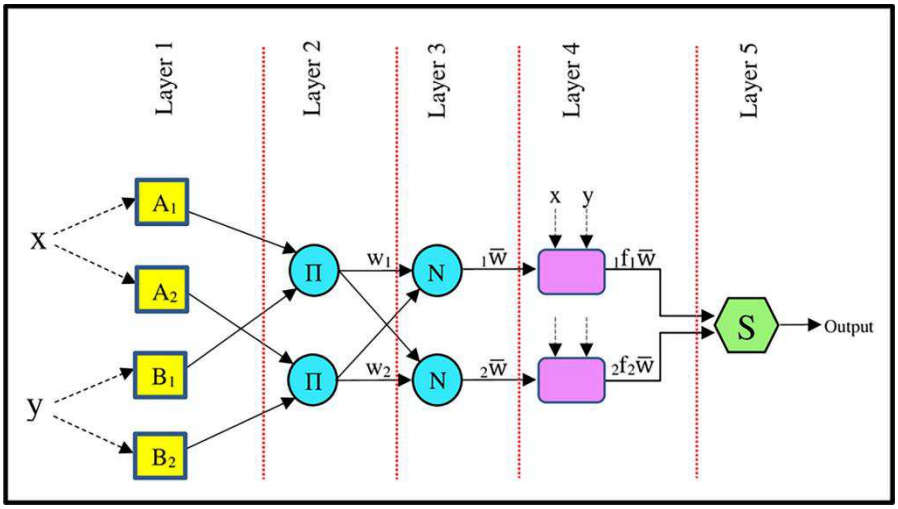

Fig. 7 Architecture of ANFIS

For this study, the ANFIS model was constructed with three inputs:
- Angle of attack: 0°, 5°, 10°, 15°, 20°
- DBD-PA force per unit length: 1.26, 5.5, 15.25 mN/m
- Actuator installation location: 2%, 10%, 30%, 70%, 90% chord

A total of 90 CFD simulations were performed to generate the training dataset. The nominal parametric grid comprises 5×3×5 = 75 combinations of actuator force level, chordwise installation position, and angle of attack. To enrich the dataset and improve the generalization of the surrogate model, 15 additional CFD cases were included at intermediate angles of attack and at intermediate chordwise positions between the five nominal stations. These auxiliary cases were selected deliberately to populate the regions where the aerodynamic coefficients vary most nonlinearly, near the stall threshold and in the immediate vicinity of the 30% chord placement limit. The data were randomly split into 75% for training and 25% for testing. The model performance was evaluated using the coefficient of determination (R^2) and mean squared error (MSE). As shown in Table 4, the best performance was achieved with 4-4-4 membership functions (4 membership functions per input), yielding R^2 values close to 1 and MSE values close to 0 for all three outputs (Cl, Cd, Cm).

A custom MATLAB based prediction tool was developed to employ the trained ANFIS model to predict aerodynamic performance at untested angles of attack and actuator positions, thereby generating a comprehensive performance dataset beyond the directly simulated conditions.

4. Results and Discussion

4.1. Effect of Plasma Actuator Strength and Position

This section presents a numerical investigation into the effects of plasma actuator intensity and placement on the suction surface of a NACA 4412 airfoil. Actuator performance was parameterized by force per unit length, with three values examined: 1.26, 5.5, and 15.25 mN/m. These actuators were positioned at five streamwise locations corresponding to 2%, 10%, 30%, 70%, and 90% of the airfoil chord length. For each location, three actuator configurations were modeled to enable a comparative analysis of their effects on the lift, drag, and pitching moment coefficients. Throughout this study, an actuator configuration is termed "optimal" when it provides the best combined improvement in lift, drag, and pitching moment across both the pre-stall and

post-stall regimes. Figure 8 illustrates representative flow fields at a 15-degree angle of attack, comparing the base case DBD-off condition (the top photo in figure 8) with three activated DBD configurations at distinct installation positions, as specified in Table 2. The velocity contours and streamlines demonstrate the modification of the flow separation behavior resulting from plasma actuation.

Table 2 Definition of actuator force levels (AG) and chordwise installation positions (ST)

Test case	Parameter	values
AG1	Low force level	1.26 mN/m
AG2	Medium force level	5.5 mN/m
AG3	High force level	15.25 mN/m
ST1	Chordwise position	2% C
ST2	Chordwise position	10% C
ST3	Chordwise position	30% C
ST4	Chordwise position	70% C
ST5	Chordwise position	90% C

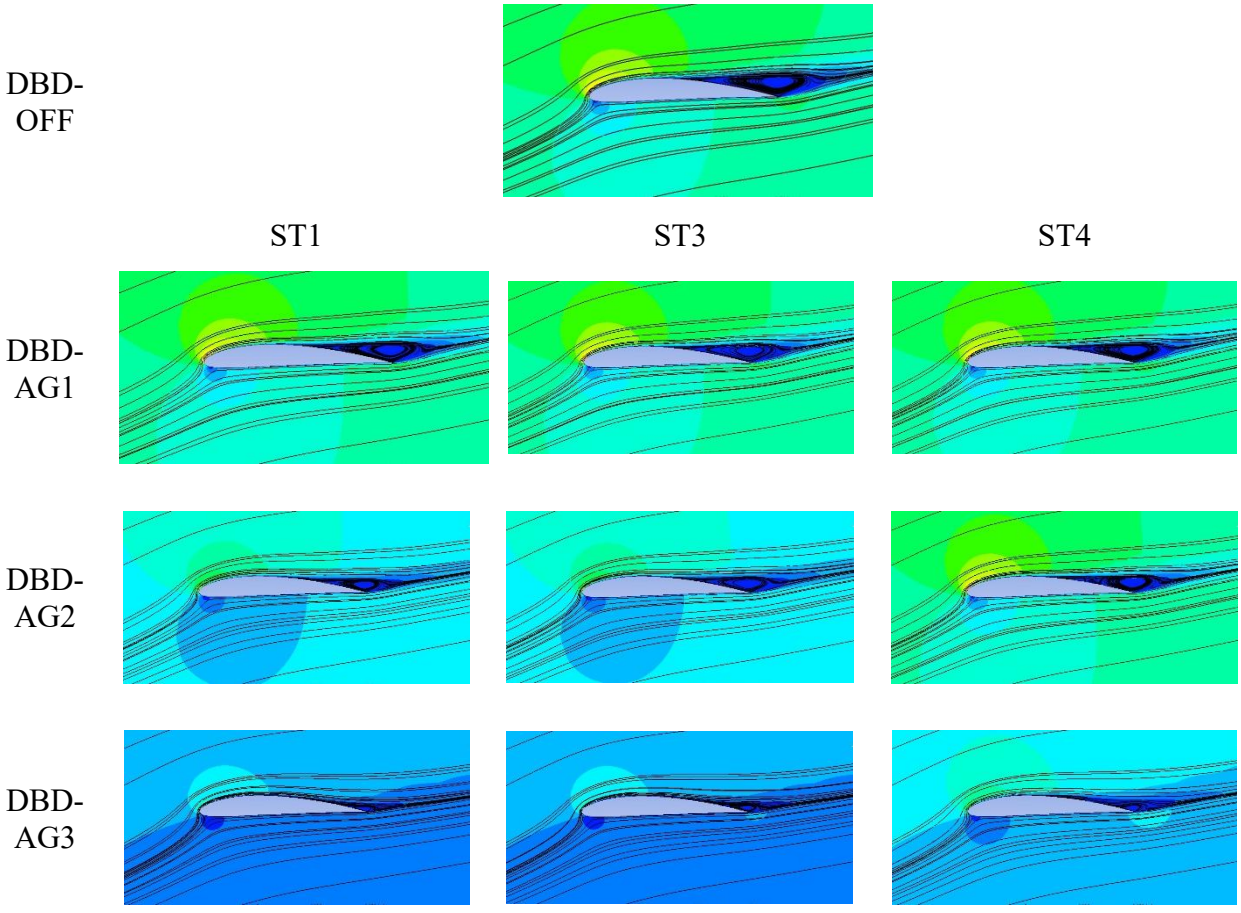

Fig. 8 Velocity contours and streamlines at AoA=15 deg. and Re=6.86×10^5. Top photo: DBD-off, the rest of the photos are three activated DBD configurations (AG1, AG2 and AG3) at three distinct installation positions (ST1, ST3 and ST4).

To comprehensively evaluate the aerodynamic performance, the qualitative flow structures (Figure 8) must be correlated with the quantitative variations in the lift (Cl), drag (Cd), and pitching moment (Cm) coefficients presented in Figure 9. The bar charts in Figure 9 compare the baseline (DBD-off) with the three actuator power levels (AG1, AG2, AG3) at three critical streamwise positions (ST1, ST3, ST4) across various angles of attack (AoA = 0°, 5°, 10°, 15°, 20°).

At low angles of attack (AoA = 0° and 5°), the flow is fully attached, and the aerodynamic coefficients are highly sensitive to the actuator's placement and voltage. As shown in Figure 9, the low-voltage actuator (AG1) produces negligible changes in Cl and Cd, which aligns with the flow visualization in Figure 8 where the flow topology remains virtually unchanged. Conversely, the high-voltage actuator (AG3) placed at the trailing edge (ST4) yields the maximum lift enhancement (approx. 15% at AoA = 5°) and a notable drag reduction. This indicates that at low angles of attack, where trailing-edge separation is the primary mechanism, rearward actuation is more effective. However, high-power leading-edge actuation (AG3 at ST1) causes a significant drag penalty (up to a 139% increase at AoA = 0°) due to the introduction of excessive momentum near the stagnation point, which disrupts the natural pressure distribution. The counterproductive behavior of trailing-edge actuation therefore emerges only once leading-edge separation dominates (AoA $\geq$ 10°), as quantified in Table 3.

As the angle of attack increases to AoA = 10°, the flow approaches the stall threshold. Figure 9 reveals that AG3 at the leading edge (ST1) and at 30% chord (ST3) begins to show superior performance compared to ST4. The Cl values for ST1 and ST3 surpass the baseline and ST4 cases, while the Cd values remain relatively low. This is directly supported by Figure 8, which shows that the medium (AG2) and high (AG3) voltage actuations at ST1 and ST3 effectively energize the boundary layer, delaying the onset of separation and maintaining a coherent shear layer.

The most striking quantitative evidence of flow control effectiveness is observed in the post-stall regime (AoA = 15° and 20°). At AoA = 15°, the high-voltage actuator (AG3) at ST1 and ST3 produces a dramatic increase in lift (up to 31% for ST1 and 26.5% for ST3) and a substantial drag reduction (approx. 28% for both). This quantitative leap is a direct consequence of the flow physics depicted in Figure 8, where the AG3 actuator completely reattaches the separated shear layer, eliminating the massive recirculation zone and significantly reducing the wake momentum deficit. At AoA = 20° (deep stall), the baseline flow suffers massive separation, but the AG3 actuator at ST1 exhibits an extraordinary 83.3% increase in lift and a 61% reduction in drag. This confirms that leading-edge actuation at high voltage provides the necessary momentum to overcome the severe adverse pressure gradient, suppressing the low-pressure vortex and restoring the suction surface pressure distribution. Conversely, despite the high voltage of AG3 at ST4, the quantitative results show a negligible lift increase at AoA = 20° (+0.4%), confirming the visual observation in Figure 8 that rearward actuation cannot suppress the dominant leading-edge separation.

Regarding the pitching moment (Cm), Figure 9 demonstrates that all actuated cases generally produce a more negative Cm compared to the baseline, with the magnitude varying based on position and angle of attack. However, at post-stall conditions (AoA = 15° and 20°), the leading-edge actuation (ST1 and ST3) mitigates the severe negative shift in Cm. For instance, at AoA = 20°, AG3 at ST1 results in a 57.7% less negative Cm compared to the off-state, which is highly beneficial for aircraft trim and stability.

Although ST1 yields a marginally higher lift gain at AoA = 15° (31.4% vs. 26.5% for ST3), its drag penalty at low-to-moderate angles of attack is substantially larger (e.g., 138.8% vs. 85.8% at AoA = 0°, and 92.4% vs. 53.9% at AoA = 5°; Table 3), and its pitching-moment improvement at

stall is less pronounced (30.0% vs. 30.2% at AoA = 15°, but −57.7% vs. −68.0% at AoA = 20°). When lift, drag, and pitching moment are considered jointly across the pre- and post-stall envelope, ST3 emerges as the optimal compromise: it retains nearly the full lift benefit of ST1 in the stall regime while avoiding the severe off-design drag and moment penalties that ST1 incurs. This multi-objective criterion, rather than peak lift in isolation, defines the optimum adopted throughout this study.

The quantitative data in Figure 9 strongly corroborate the physical flow mechanisms visualized in Figure 8. The combination of high voltage (AG3) and optimal leading-edge placement (ST3) is unequivocally identified as the most effective strategy for controlling massive flow separation and maximizing aerodynamic efficiency in stall and post-stall regimes.

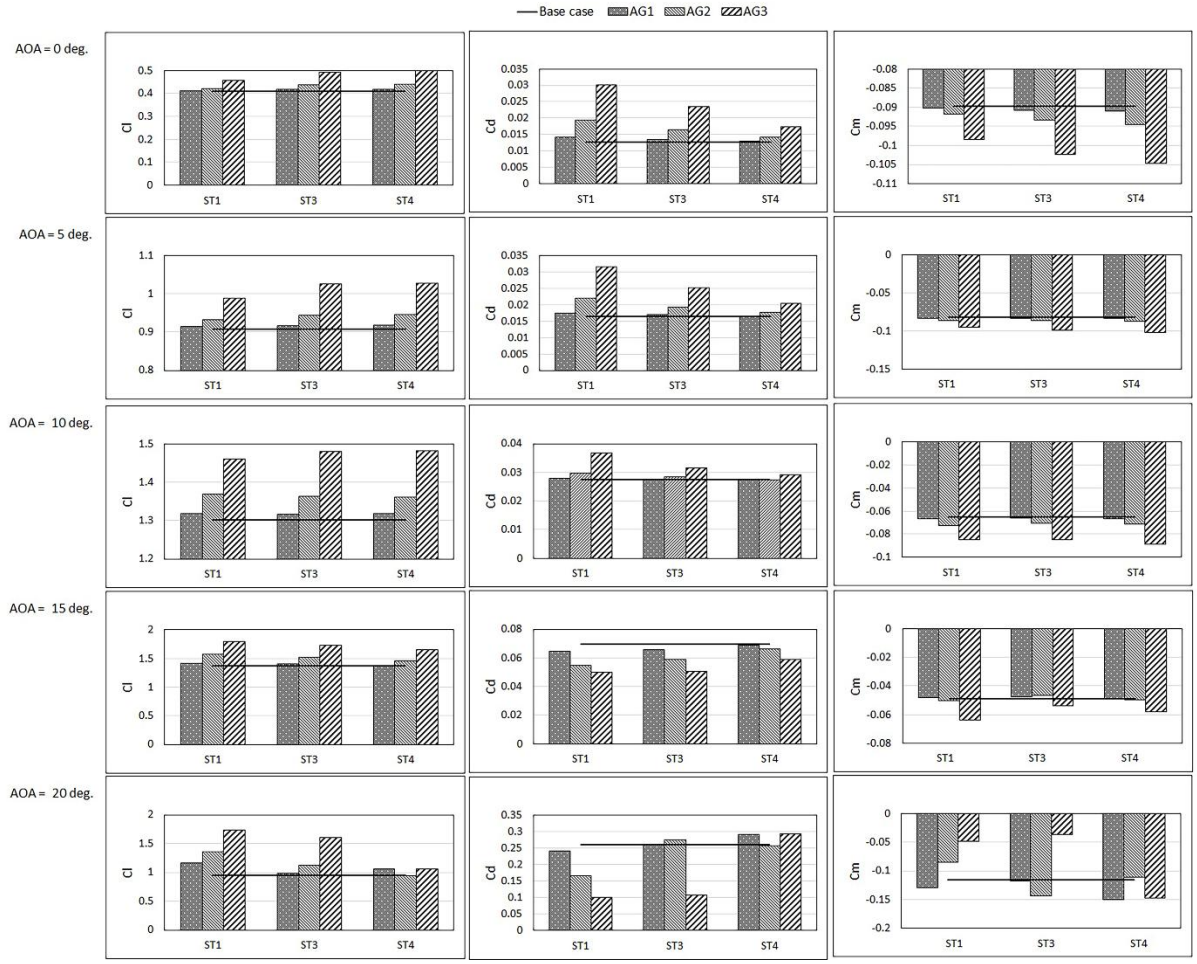

Fig. 9 Cl, Cd and Cm at various AoA (0, 5, 10, 15 and 20 degree), Actuator status (AG1, AG2 and AG3) and actuator positions (ST1, ST3 and ST4)

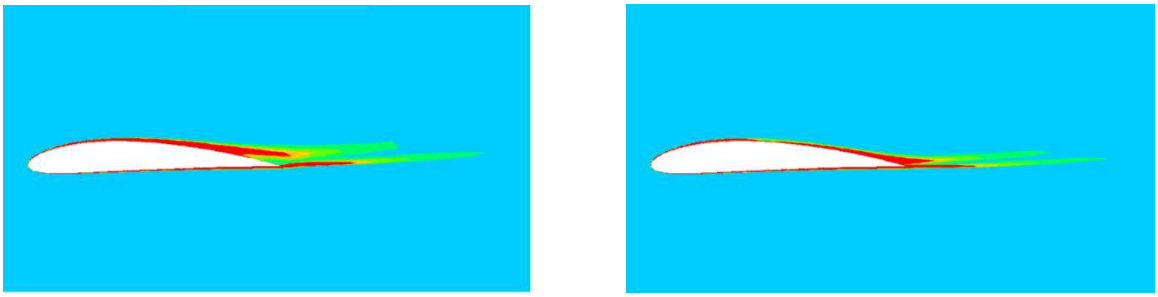

(a) AoA=10 deg.

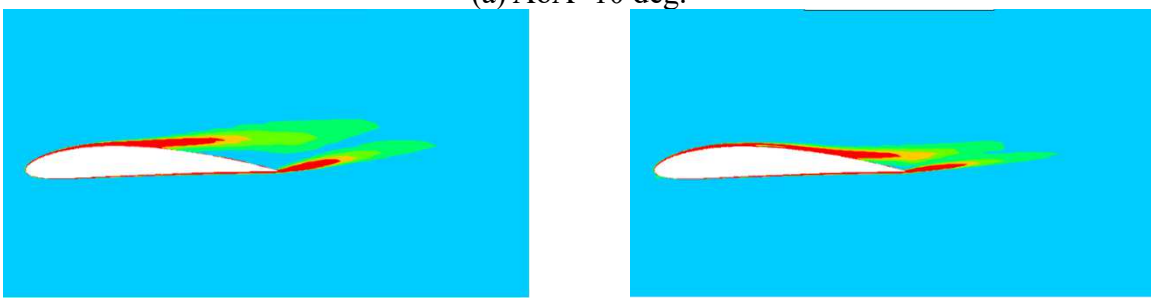

(b) AoA=15 deg.

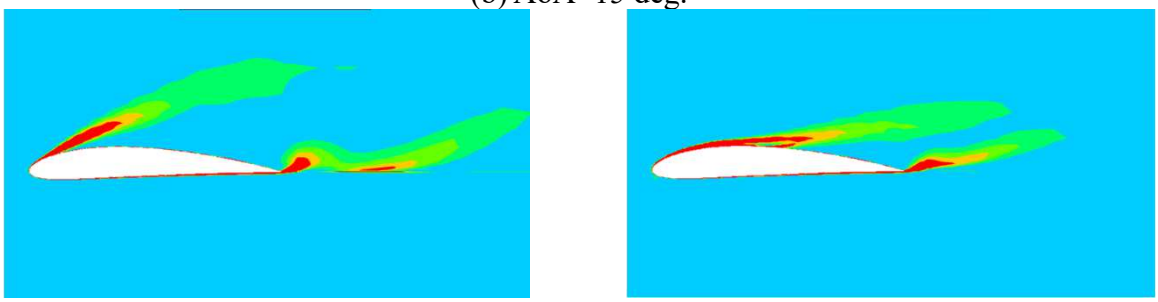

(c) AoA=20 deg.

Fig. 10 Comparison of vorticity contours at different angles of attack. (Left) DBD-0ff (Right) AG3 plasma actuator at ST3 position

Figure 10 provides deeper insight into the underlying physical mechanisms by comparing the vorticity contours of the baseline (DBD-off) and the optimal plasma actuation configuration (AG3 at ST3) at different angles of attack (AoA = 10°, 15°, 20°). At the pre-stall condition (AoA = 10°), the baseline flow remains mostly attached, with a thin, concentrated shear layer originating near the leading edge and trailing off the surface (Figure 10a, left). Activating the high-voltage AG3 actuator at the 30% chord position (Figure 10a, right) introduces momentum into the boundary layer, which slightly delays the transition and reduces the vorticity magnitude in the near-wall region, explaining the corresponding lift increase and drag reduction observed in Figure 9.

As the angle of attack increases to the stall threshold (AoA = 15°), the baseline flow experiences severe separation. A prominent shear layer detaches from the leading edge, and a secondary vortex structure forms near the trailing edge (Figure 10b, left). However, with the AG3 actuator engaged (Figure 10b, right), the flow topology is fundamentally altered. The leading-edge low-pressure vortex is suppressed, and the controlled flow field exhibits a reduced separated region and a modified shear-layer trajectory. The vorticity contour exhibits a much thinner and more coherent layer, eliminating the massive recirculation zone. This physical restructuring of the shear layer directly corresponds to the 26.5% increase in maximum lift and 27.6% drag reduction quantified in Figure 9.

The most dramatic flow control effect is observed at the deep post-stall condition (AoA = 20°). In the baseline case (Figure 10c, left), the flow field is dominated by a massive, highly turbulent low-pressure vortex near the leading edge, accompanied by an unsteady wake and a strong secondary vortex. This complete detachment causes the severe reduction in lift and the increase in drag seen in Figure 9. In stark contrast, the AG3 actuation at ST3 (Figure 10c, right) remarkably restores the flow attachment. The dominant leading-edge vortex is attenuated, and the shear layer is maintained closer to the surface, resulting in a significantly narrower wake. Figure 10 confirms that the superior aerodynamic performance achieved by the AG3 actuator at ST3 is not merely a result of added momentum, but stems from its ability to reshape the separated shear layer into a thinner, more coherent structure that prevents the catastrophic growth of leading-edge vortices in the stall and post-stall regimes.

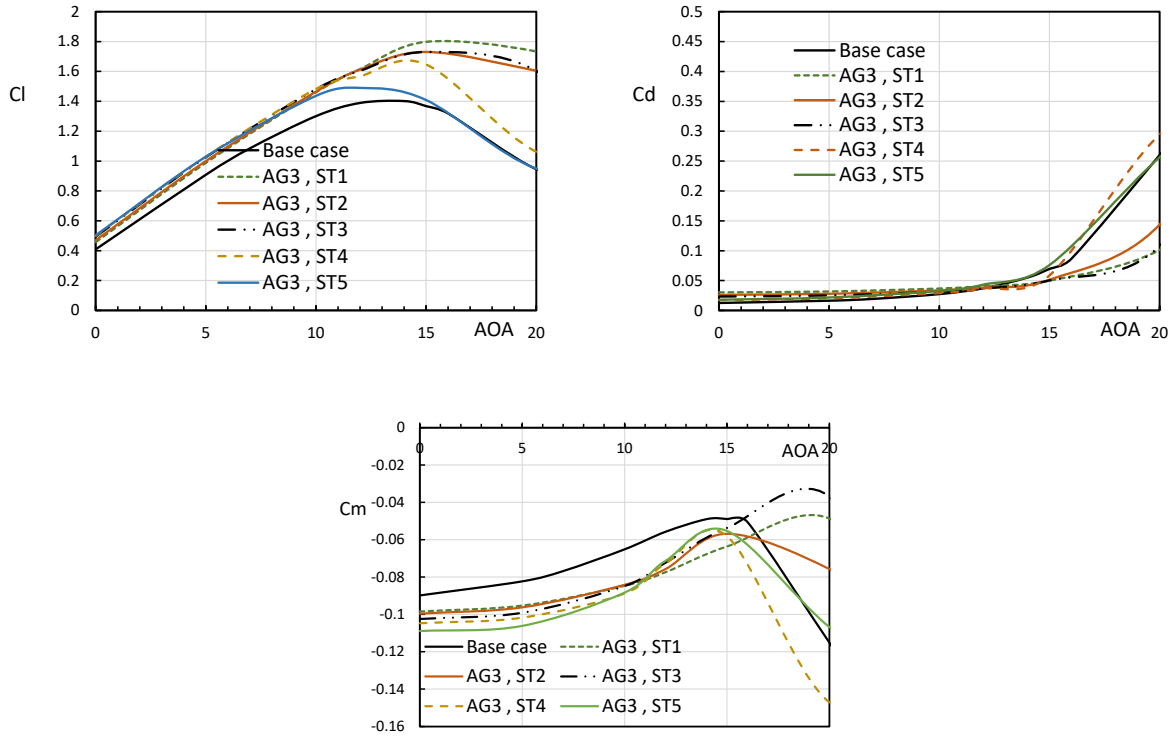

Fig. 11 Effect of chordwise installation position of the high-voltage AG3 actuator (ST1–ST5) on the aerodynamic coefficients (Cl, Cd and Cm) across the pre- and post-stall regimes.

Figure 11 delineates the optimal placement strategy across the entire flight envelope. As observed in the lift coefficient (Cl) plot, the baseline airfoil reaches its maximum lift at approximately AoA = 14° before stalling sharply. Up to AoA = 10°, all actuated cases slightly improve lift, but the curves remain tightly clustered, indicating that actuation placement is less critical in the fully attached regime. However, in the post-stall regime (AoA > 15°), the aerodynamic response diverges significantly based on the installation position. The rearward placements, particularly ST5, show a precipitous drop in lift, performing even worse than the baseline at AoA = 20°. In contrast, the forward placements (ST1, ST2, and ST3), effectively delay stall and maintain a high

lift plateau up to AoA = 20°. The ST1 and ST2 configurations yield the highest maximum lift and the most delayed stall angle.

The drag coefficient (Cd) plot corroborates this behavior. While drag remains nearly identical for all cases at low angles of attack, it increases exponentially beyond AoA = 15° for the baseline and rearward-placed actuators (ST4 and ST5). However, leading-edge actuation (ST1, ST2, and ST3) effectively suppresses this drag rise. At the deep post-stall region, the ST1 configuration achieves the lowest drag among all actuated cases, directly linking to the shear layer reattachment mechanism observed in Figure 10. The poor performance of ST5 at high angles is consistent with the physical observation in Figure 8, where downstream actuation fails to prevent the dominant leading-edge separation.

The pitching moment coefficient (Cm) plot reveals a critical trade-off. In the pre-stall regime (AoA < 10°), all actuated cases yield a more negative Cm compared to the baseline, which could negatively impact trim stability. However, as the flow approaches and exceeds stall (AoA > 15°), the baseline Cm drops sharply (becoming more negative) due to massive separation. The forward-placed actuators (ST1, ST2 and ST3) counteract this detrimental shift, maintaining a more positive (less negative) pitching moment. Interestingly, the rearward ST4 and ST5 placements cause a sharp positive divergence in Cm near AoA = 20°, which is indicative of the uncontrolled shedding of trailing-edge vortices and an unstable wake structure.

Percentage changes for all coefficients and positions are summarized in Table 3. A negative sign in Cd indicates a decrease in drag, and a negative sign in Cm indicates that it becomes more positive.

Table 3 The percentage variations in lift, drag, and pitching moment coefficients for the AG3 actuator configurations compared to the unactuated base case

	AOA	0	5	10	15	20
%ΔCl	ST1	11.9	8.8	12.3	31.4	83.3
	ST2	14.9	10.1	12.6	26.5	69.6
	ST3	20.7	12.9	13.9	26.5	69.6
	ST4	22.0	13.3	14.0	20.3	12.3
	ST5	23.0	13.3	10.4	2.9	0.4
%ΔCd	ST1	138.8	92.4	33.2	-28.4	-61.1
	ST2	107.7	70.3	22.5	-26.0	-44.7
	ST3	85.8	53.9	14.8	-27.6	-58.5
	ST4	38.0	24.6	5.9	-15.7	13.3
	ST5	41.0	31.6	18.0	8.9	-1.4
%ΔCm	ST1	9.6	15.8	30.0	30.0	-57.7
	ST2	10.9	16.9	29.2	16.1	-34.2
	ST3	14.0	20.4	30.2	9.7	-68.0
	ST4	16.6	23.6	36.3	18.7	27.8
	ST5	21.2	28.9	35.5	13.0	-7.3

4.2. Evaluation of ANFIS Results

Numerical simulations were conducted across three plasma actuator power levels (AG1, AG2, AG3), five streamwise installation positions (ST1–ST5), and five angles of attack (0°, 5°, 10°, 15°,

and 20°). To efficiently predict aerodynamic performance at untested parameters—including intermediate angles of attack and actuator mounting positions—an Adaptive Neuro-Fuzzy Inference System (ANFIS) model was developed and validated. The reliability of the ANFIS predictions was quantitatively assessed using the coefficient of determination (R^2) and mean squared error (MSE), where an R^2 value close to 1 and an MSE approaching zero indicate high predictive accuracy [41]. Following review-article recommendations, 75% of the available data were allocated for training and the remaining 25% for testing [42-43].

As detailed in Table 4, four different grid partition configurations with varying numbers of membership functions (2-2-2, 3-3-3, 4-4-4, and 5-5-5) were evaluated. The input membership function type was Gaussian, and the output membership function was linear. Training and testing performance were evaluated independently for all configurations. The best overall performance was achieved with the 4-4-4 configuration (resulting in 64 fuzzy rules), which yields high predictive accuracy for lift and drag in both training ($R^2 \approx 1.000$) and testing ($R^2 = 0.966$ for Cl, $R^2 = 0.847$ for Cd). The pitching-moment coefficient, however, exhibits a lower testing accuracy ($R^2 = 0.736$). This behavior is physically expected rather than a deficiency of the surrogate: Cm is governed by the global pressure distribution and is highly sensitive to the exact location of shear-layer reattachment and vortex shedding, which change abruptly near and beyond stall (AoA ≥ 15°). With only 90 CFD samples, the test subset contains relatively few post-stall points, making Cm the most data-hungry output.

Crucially, this limitation does not undermine the optimization conclusions, for two reasons. First, the optimization objective is dominated by Cl and Cd, for which the surrogate is highly reliable. Second, the ANFIS-predicted optimum was not accepted on the basis of the surrogate alone; it was independently verified by a dedicated CFD simulation (Figure 13). Therefore, the lower Cm accuracy affects only the quantitative smoothness of the Cm trend in Figure 14, not the identity or validity of the optimal actuator configuration.

Furthermore, as illustrated in the scatter plots of Figure 12, the notable agreement between the actual data (open circles) and the ANFIS output (cross marks) visually confirms the model's consistency and robustness in both the training and testing phases. Following this successful validation, the ANFIS model was employed as a reliable surrogate to generate a comprehensive dataset of aerodynamic coefficients for conditions not explicitly covered by the numerical simulations.

Table 4 Evaluation of ANFIS results at various Membership Function

MF	Data Type	Cl		Cd		Cm	
		R2	MSE	R2	MSE	R2	MSE
222	Training	0.998	0.0192	0.999	0.0047	0.961	0.0059
	Test	0.935	0.1047	0.832	0.0545	0.669	0.0211
	All	0.983	0.0496	0.966	0.0246	0.877	0.0108
333	Training	1.000	0.0020	1.000	0.0002	1.000	0.0003
	Test	0.845	0.1500	0.804	0.0641	0.519	0.0425
	All	0.969	0.0667	0.956	0.0285	0.729	0.0189
444	Training	1.000	0.0000	1.000	0.0000	1.000	0.0000
	Test	0.966	0.0800	0.847	0.0516	0.736	0.0550
	All	0.992	0.0355	0.971	0.0229	0.859	0.0245

555	Training	1.000	0.0000	1.000	0.0000	1.000	0.0000
	Test	0.809	0.2863	0.732	0.1256	0.593	0.1140
	All	0.912	0.1272	0.873	0.0558	0.772	0.0507

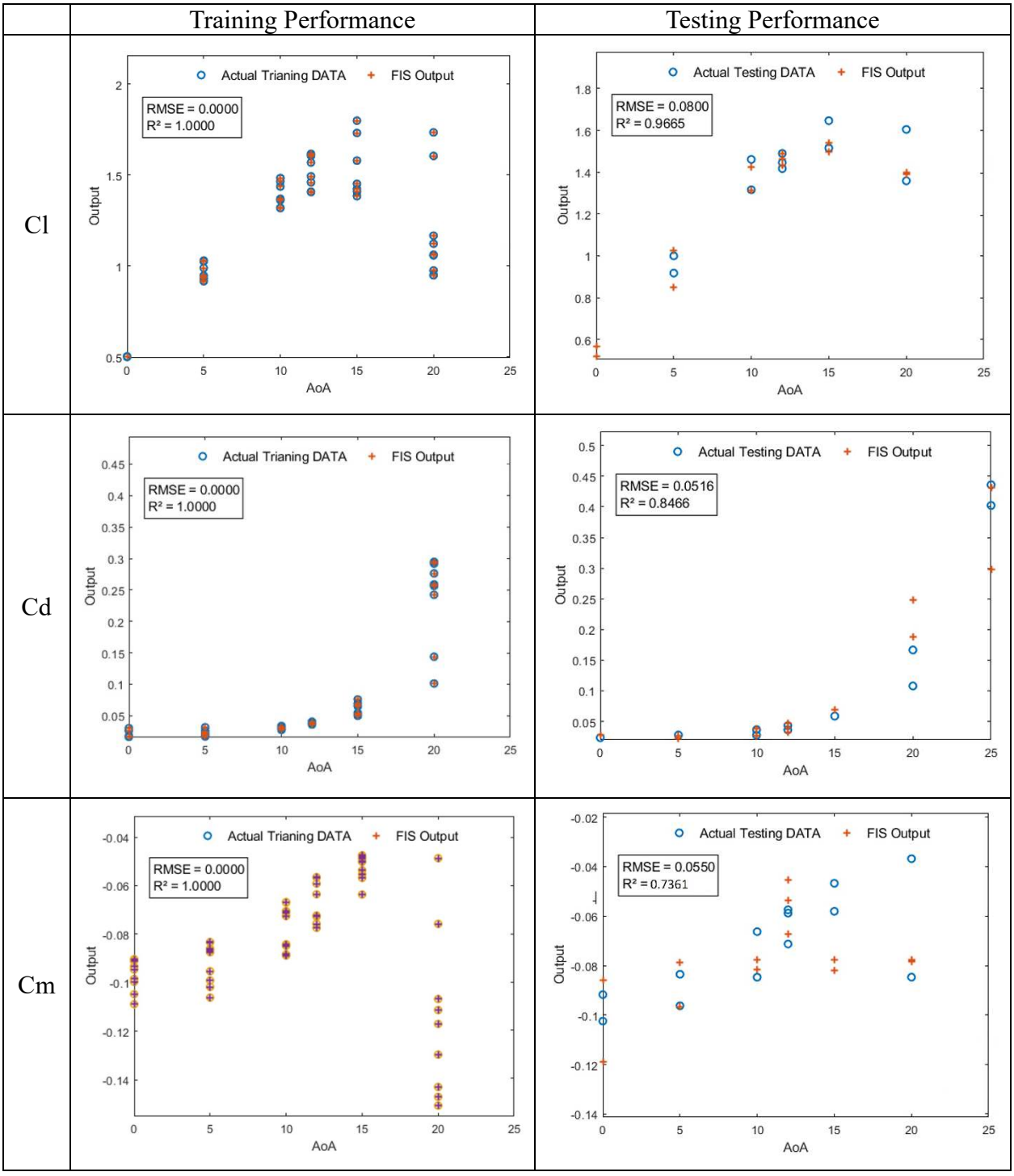

Fig. 12 Consistency of ANFIS with the actual results

Figures 13 and 14 demonstrate the capability of the adaptive ANFIS to accurately predict aerodynamic performance under conditions that have not been explicitly numerically simulated.
Figure 13 presents the aerodynamic performance predictions obtained from the adaptive ANFIS model for the AG3 plasma actuator under different conditions. The figure is structured into two main columns. The left column (AG3, ST2) is dedicated to validating the reliability of the ANFIS framework. The ANFIS model predicts aerodynamic coefficients across the entire range of angles of attack, including angles for which no numerical simulation was performed. At the specific angles where CFD data points exist, the ANFIS predictions demonstrate excellent agreement with the discrete numerical results, validating the high accuracy of the surrogate model. As observed in the left panels, the ANFIS model (solid line) closely matches the numerical data across all three aerodynamic coefficients: Lift (Cl), Drag (Cd), and Pitching Moment coefficient (Cm).
The right column displays the ANFIS-predicted aerodynamic coefficients for the AG3 actuator positioned at various chordwise locations: 5%, 25%, 65%, and 85% of the airfoil chord (c). These predictions highlight the profound impact of actuator placement on aerodynamic performance. While the actuators located at 5% and 25% chord exhibit consistent and favorable aerodynamic trends, the configurations at 65% and 85% chord result in severe performance degradation. Specifically, as the angle of attack increases, the rearward placements (65% and 85% c) show a marked reduction in maximum lift, a sharp and abrupt increase in drag, and a significant nonlinear shift towards more negative pitching moments, indicating the onset of premature separation and loss of control effectiveness.
Figure 14 illustrates the effect of varying the plasma actuator installation position along the chord on the aerodynamic performance of the airfoil, as predicted by the ANFIS model across different angles of attack. This comprehensive parametric sweep provides critical insights into the optimal actuator location and its underlying flow control mechanisms.
As observed in the lift and drag coefficient (top panels), the actuator's effectiveness is highly sensitive to its chordwise position. At lower angles of attack (e.g., AoA = 0° and 5°), the lift remains relatively insensitive to placement. However, at higher angles of attack (AoA = 10°, 15°, and 20°), a distinct threshold emerges at approximately 30% chord. Up to this 30% limit, the plasma actuator effectively energizes the boundary layer, mitigating flow separation and yielding a significant enhancement in lift and a simultaneous reduction in drag. Conversely, when the actuator is positioned beyond 30% chord (towards the trailing edge), the Cl drops precipitously, and the Cd experiences a sharp, nonlinear increase. This confirms that actuation aft of the 30% chord is too far downstream to suppress the dominant leading-edge separation, rendering the control strategy ineffective and even detrimental. It should be emphasized that this 30% chord threshold is identified from the joint behavior of Cl, Cd, and Cm rather than from maximum lift alone: actuator positions closer to the leading edge (5–10% chord) can produce slightly higher peak lift at stall, but they do so at the cost of a markedly larger drag penalty in the attached-flow regime and a less favorable pitching-moment recovery at deep stall (Figure 14 and Table 3). The 30% chord location therefore represents the best overall trade-off across the entire operating envelope.
The pitching moment coefficient (bottom panel) further corroborates this critical placement limit. While the Cm variations are minimal for actuator positions below 30% chord, a drastic and nonlinear positive shift in Cm is observed for AoA = 20° at post-stall condition, when the actuator is moved between 40% and 60% chord. This abrupt change is indicative of a fundamental alteration

in the pressure distribution and the wake structure, likely due to the premature and uncontrolled separation of the shear layer caused by the poorly positioned actuator.

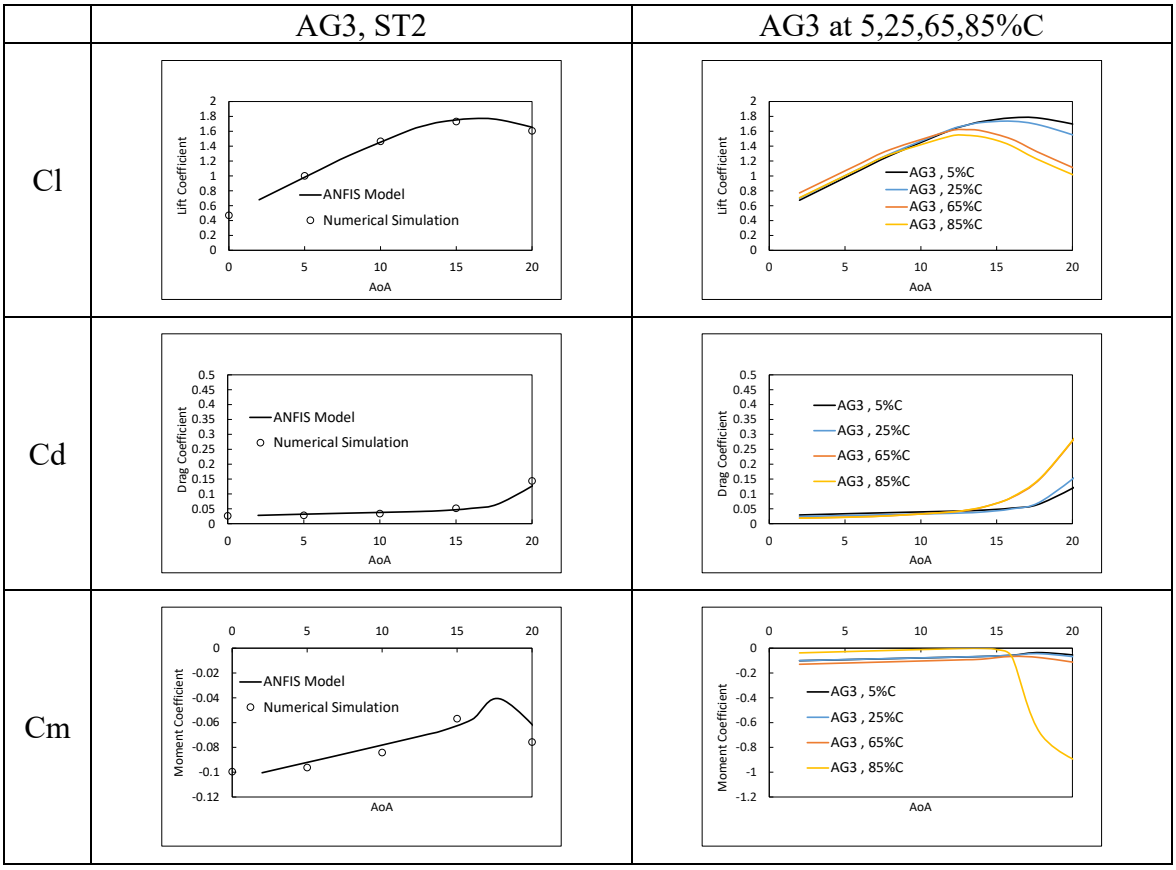

Fig. 13 Cl, Cd and Cm versus angle of attack by ANFIS prediction and comparison with numerical results

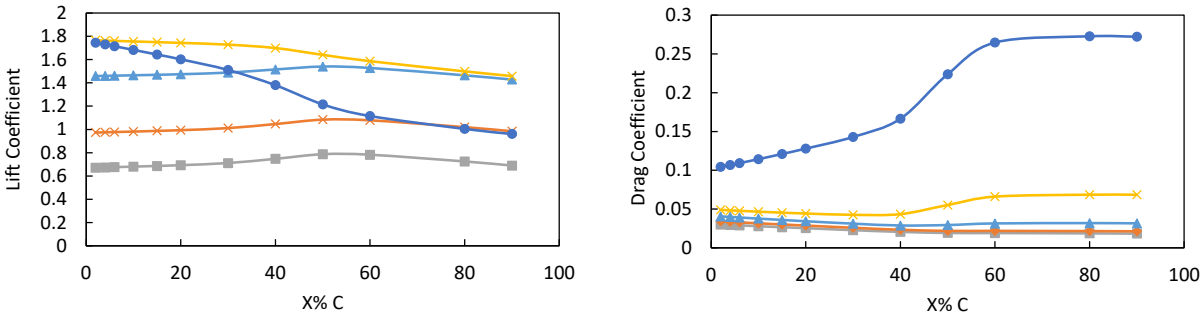

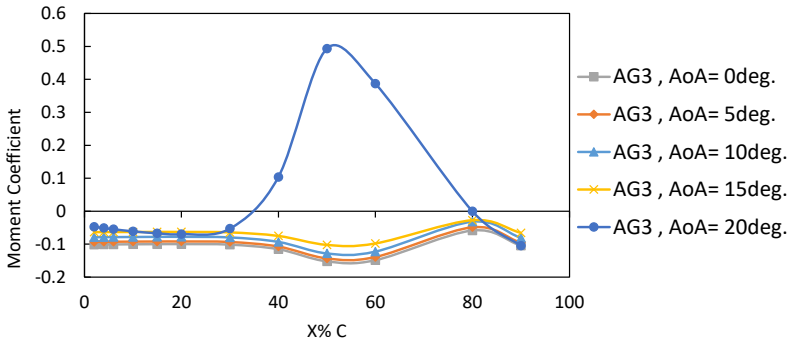

Fig. 14 The effect of changing the plasma actuator installation position on the aerodynamic performance of the airfoil

5. Conclusion

This study investigated active flow control on a NACA 4412 airfoil using DBD plasma actuators. A hybrid CFD-ANFIS framework was developed to optimize actuator parameters. The main conclusions are as follows:

1. Optimal DBD plasma actuation at Re = 6.86×10^5 is achieved with a 10 kV actuator placed at 30% chord on the suction surface when lift, drag, and pitching moment are optimized jointly.
2. Two distinct lift-enhancement mechanisms were identified depending on the flow regime: at low AoA (fully attached flow), rearward actuation (≈70% chord) energizes the trailing-edge boundary layer and yields the largest lift gain; at high AoA (stall/post-stall), leading-edge actuation (≈10–30% chord) attenuates the leading-edge low-pressure vortex and reattaches the separated shear layer, whereas rearward actuation becomes ineffective or detrimental.
3. Under stall conditions (AoA = 15°), the optimal configuration (AG3 at ST3) produced a 26.5% increase in maximum lift, a 27.6% drag reduction, and an improved pitching moment by reshaping the separated shear layer into a thinner, coherent structure.
4. The ANFIS surrogate reproduced the CFD trends with $R^2 > 0.96$ (training) and $R^2 > 0.84$ (testing) for Cl and Cd, while Cm showed a more limited test accuracy ($R^2 \approx 0.74$) due to post-stall sensitivity.

The study is limited to two-dimensional URANS simulations, which may not fully capture 3D flow structures and unsteady vortex dynamics. Future work should extend the framework to 3D configurations and experimental validation.

The optimized control strategy can contribute to enhanced range, endurance, and fuel efficiency in aerospace applications.

References

1. Ab Satar, M.H., Razak, N.A., Abdullah, M.S., Ismal, F. A comprehensive comparison of passive flow controls on the wind turbine blade lift and drag performances: A CFD approach. *Eur. J. Mech. B Fluids*, **108**, 119-133; 10.1016/j.euromechflu.2024.07.009 (2024)

2. Carlos, J., Matias-Garcia, R., Sebastián, B., Barderas, F.E. Experimental comparison of flow control techniques on helicopter flight deck of frigates. *AIAA Aviation* 2023 Forum; 10.2514/6.2023-4207 (2023).

3. Md Abdullah, Galib, M.T., Md Ali Khan, S., Rahman, T., Md Hossain, M. Recent advancements in flow control using plasma actuators and plasma vortex generators. *Heat Transf*. **53**, 4244-4267; 10.1002/htj.23131 (2024).

4. Veerakumar, R., Raul, V., Liu, Y. et al. Metamodeling-based parametric optimization of DBD plasma actuation to suppress flow separation over a wind turbine airfoil model. *Acta Mech. Sin*. **36**, 260–274; 10.1007/s10409-020-00951-6 (2020).

5. Inasawa, A., Kagawa, Y. Control of trailing-edge noise from airfoil using a plasma actuator. *J. Fluid Sci. Technol*. **13**; 10.1299/jfst.2018jfst0003 (2018).

6. Sun, Z., Shi, Z., Zhang, W., Sun, Q., Sun, Q. and Li, Z. Numerical Investigation on Flow Control of a Hypersonic Airfoil by Plasma Synthetic Jet. *J. Aerosp. Eng.* **35**; 10.1061/(ASCE)AS.1943-5525.0001467 (2022).

7. Sundaram, P., et al. Flow control using single dielectric barrier discharge plasma actuator for flow over airfoil. *Phys. Fluids* **34**; 10.1063/5.0107638 (2022).

8. Pouryoussefi, S.G., Mirzaei, M., Hajipour, M. Experimental study of separation bubble control behind a backward-facing step using plasma actuators. *Acta Mech*. **226**, 1153–1165; 10.1007/s00707-014-1245-7 (2015).

9. Khoshkhoo, R., Jahangirian, A. Numerical simulation of flow separation control using multiple DBD plasma actuators. *J. Appl. Fluid Mech*. **9,** 1865–1875; 10.18869/acadpub.jafm.68.235.25325 (2016).

10. Corke, T.C., Post, M.L., Orlov, D.M. Single dielectric barrier discharge plasma enhanced aerodynamics physics, modeling and applications. *Exp. Fluids* **46**, 1–26; 10.1007/s00348-008-0582-5 (2009).

11. Rahni, A., Jahangirian, A. Multi-Objective Optimization of DBD Plasma Actuator Characteristics for Turbulent Flow Separation Control over Airfoils. *Flow Meas. Instrum*. **105**; 10.1016/j.flowmeasinst.2025.102951 (2025).

12. Chae, J., Ahn, S. & Kim, K.H. Reduced Kinetic Model for ns-DBD Plasma Actuators at Atmospheric Pressure. *Int. J. Aeronaut. Space Sci*. **27**, 2719–2735; 10.1007/s42405-026-01123-9 (2026).

13. Roy, S., Wang, C.C. Bulk flow modification with horseshoe and serpentine plasma actuators. J. Phys. D Appl. Phys. **42**; 10.1088/0022-3727/42/3/032004 (2009).

14. Wang, L., Wong, C.W., Md Mahbub Alam, Zhou, Y. Post-stall fl ow control using a sawtooth plasma actuator in burst mode. *Aerosp. Sci. Tech*. **107**; 10.1016/j.ast.2020.106251 (2020).

15. Ünal, N., Oz, Y., Ünal, E.A., Oktay, T. Enhancing aerodynamic performance of a two-dimensional airfoil using plasma actuators. *Aerosp. Sci. Tech*. **158**; 10.1016/j.ast.2024.109882 (2025).

16. Jukes, T.N., Choi, K.S. Control of unsteady flow separation over a circular cylinder Using dielectric-barrier-discharge surface plasma. *Phys. Fluids* **21**; 10.1063/1.3237151 (2009).

17. Zhang, X., et al. Turbulent boundary layer separation control using plasma actuator at Reynolds number 200000. *Chin. J. Aeronaut*. **29**, 1237–1246; 10.1016/j.cja.2016.08.006 (2016).

18. Daud, N., Kozato, Y., Kikuchi, S., Imao, S. Control of leading edge separation on airfoil using DBD plasma actuator. *J. Fluid. Sci. Technol*. **9**; 10.1299/jfst.2014jfst0049 (2014).

19. Mahdavi, H., Daliri, A., Sohbatzadeh, F., Shirzadi, M., Rezanejad, M. A single unsteady DBD plasma actuator excited by applying two high voltages simultaneously for flow control. *Phys. Plasmas*, **27**; 10.1063/5.0010069 (2020).

20. Tang. M., Tang. J., Zhou. D., Yu. D. Dielectric barrier discharges in airflow around a circular cylinder. *Phys. Plasmas* **28**; 10.1063/5.0048081 (2021).

21. Chen, Z., Wen, C.Y. Flow control of a D-shaped bluff body using different DBD plasma actuators. *J. Fluid. Struct*. **103**; 10.1016/j.jfluidstructs.2021.103292 (2021).

22. Taleghani, A.S., Shadaram, A., Mirzaei, M. Effects of duty cycles of the plasma actuators on improvement of pressure distribution above a NLF0414 Airfoil. *IEEE Trans. Plasma Sci*. **40**, 1434–1340; 10.1109/TPS.2012.2187683 (2012).

23. Yarusevych, S., Kotsonis, M. Steady and transient response of a laminar separation bubble to controlled disturbances. *J. Fluid Mech*. **813**, 955–990; 10.1017/jfm.2016.848 (2017).

24. Bei, L., Hua, L., Zhonghua, H., Yinghong, L., Fei, L., Jiangbo, C., Zhiwen, D. Numerical research on airfoil transition delay by alternative current dielectric barrier discharge actuation. *Chinese J. Aeronaut*. **34**, 441–453; 10.1016/j.cja.2020.06.002 (2021).

25. Phan, M.K., Shin, J. Numerical investigation of aerodynamic flow actuation produced by surface plasma actuator on 2D oscillating airfoil. *Chin. J. Aeronaut*. **29**, 882–892; 10.1016/j.cja.2016.06.004 (2016).

26. Abdelraouf, H., Elmekawy, A.M.N., Kassab, S.Z. Simulations of flow separation control numerically using different plasma actuator models. *Alex. Eng. J*. **59**, 3881–96; 10.1016/j.aej.2020.06.044 (2020).

27. Huang, G., Dai, Y., Yang, C., Wu, Y., Xia, Y. Effect of dielectric barrier discharge plasma actuator on the dynamic moment behaviour of pitching airfoil at low Reynolds number. *Phys. Fluids* **33**; 10.1063/5.0048235 (2021).

28. Kayvanpour, R., Noori, S., Sepahvand, P. Numerical investigation of flow control using plasma actuator to improve aerodynamic characteristics of a pitching airfoil. *J. Braz. Soc. Mech. Sci. Eng.* **45**; 10.1007/s40430-023-04087-z (2023).

29. Zavarian, Z., Abdizadeh, G.R. and Noori, S. Numerical investigation of the effect of dielectric barrier discharge plasma actuator-induced momentum jet parameters on flow control of an oscillating wind turbine airfoil. *Phys. Fluids* **35**; 10.1063/5.0153485 (2023).

30. Yu, H., Zheng, J. Investigation of fl ow separation control over airfoil using nanosecond pulsed plasma actuator. *Int. J. Heat Mass Transf*. **203**; 10.1016/j.ijheatmasstransfer.2022.123786 (2023).

31. Dong, H., Xia, T., Chen, L., Liu, S., Cui, Y.D., Khoo, B.C., Zhao, A. Study on flow separation and transition of the airfoil in low Reynolds number. *Phys. Fluids* **31**; 10.1063/1.5118736 (2019).

32. Storms, B.L. and Jang, C.S. Lift Enhancement of an Airfoil Using a Gurney Flap and Vortex Generators. *J. Aircr*. **31** (1994).

33. Shyy, W., Jayaraman, B., Andersson, A. Modeling of glow discharge-induced fluid dynamics. *J. Appl. Phys*. **92**, 6434–43; 10.1063/1.1515103 (2002).

34. Jayaraman, B., Shyy, W. Modeling of dielectric barrier discharge-induced fluid dynamics and heat transfer. *Prog. Aerosp. Sci*. **44**, 139–191 (2008).

35. Karthikeyan, K.V., Harish, R. Enhanced aerodynamic performance of NACA4412 airfoil through integrated plasma actuator and Gurney flap flow control. *Results Eng*. **25**; 10.1016/j.rineng.2025.103977 (2025).

36. Roth, J.R., Sherma, D.M., Wilkinson, S.P. Boundary layer flow control with a one atmosphere uniform glow discharge surface plasma. *36th Aerospace Sciences Meeting & Exhibit*, AIAA 98-0328, Reno, NV (1998).

37. Jang, J.S.R. ANFIS: adaptive-network-based fuzzy inference system, *IEEE Trans. Syst. Man Cybern.* **23**; 10.1109/21.256541 (1993).

38. Kurnaz, S., Cetin, O., Kaynak, O. Adaptive neuro-fuzzy inference system based autonomous flight control of unmanned air vehicles. *Expert Syst. Appl*. **37**, 1229–34; 10.1016/j.eswa.2009.06.009 (2010).

39. Roy, A.G. and Peyada, N.K. Aircraft parameter estimation using Hybrid Neuro Fuzzy and Artificial Bee Colony optimization (HNFABC) algorithm. *Aerosp. Sci. Technol*. **71**, 772-782; 10.1016/j.ast.2017.10.030 (2017).

40. Guerra, M.I.S., et al. Survey on adaptative neural fuzzy inference system (ANFIS) architecture applied to photovoltaic systems. *Energy Syst*. **15**, 505–541; 10.1007/s12667-022-00513-8 (2024).

41. Patel, M., Parekh, F. Forecasting of flood flow of Panam river basin using adaptive neuro-fuzzy inference system (ANFIS) and ANN with comparative study. *J. Adv. Res. Appl. Sci. Eng. Technol*. **32**, 346–359; 10.37934/ARASET.32.2.346359 (2023).

42. Kale, S. Development of an adaptive neuro-fuzzy inference system (ANFIS) model to predict sea surface temperature (SST). *Oceanol. Hydrobiol. Stud*. **49**, 354–373; 10.1515/ohs-2020-0031 (2020).

43. Mehrabi, M., Pesteei, S.M. An adaptive neuro-fuzzy inference system (ANFIS) modelling of oil retention in a carbon dioxide air-conditioning system. *International Refrigeration and Air Conditioning Conference*. USA, 2010. URL (2010).

Funding Declaration:
This research received no external funding.

Data Availability
The data that support the findings of this study are available from the corresponding author upon reasonable request.

Author Contributions
The sole author (M.B.) was responsible for all aspects of this work, including conceptualization, methodology, software simulation, data analysis, and writing the manuscript.